Sensors & Actuators: A. Physical 349 (2023) 114085

Contents lists available at ScienceDirect

Sensors and Actuators: A. Physical

journal homepage: www.journals.elsevier.com/sensors-and-actuators-a-physical

A six dimensional dynamic force/moment measurement platform based on matrix sensors designed for large equipment

Chengbo Zhou [a,b], Mingyi Xia [a,*], Zhenbang Xu [a,b,**]

[a] Changchun Institute of Optics, Fine Mechanics and Physics, Chinese Academy of Science, Jilin, Changchun 130033, China
[b] Center of Materials Science and Optoelectronics Engineering, University of Chinese Academy of Sciences, Beijing 100049, China

ARTICLE INFO

Keywords:
Vibration
Heavy load
Matrix sensors
D optimization
Full regression method

ABSTRACT

A six-dimensional force measuring device is proposed applicable to large sources of vibration in spacecraft. Firstly, a matrix of sensors is used in the construction to improve the load capacity, mounting dimensions and stiffness of the platform. Additionally, D optimization is introduced to improve the measuring accuracy. Then, aiming to avoid the disadvantages that occur in traditional decoupling, six-dimensional forces decoupling expressions are obtained based on the full regression linear decoupling algorithm. The results of the experiment indicate that the platform has good performance in terms of load capacity (520 kN) and stiffness (fundamental frequency of 2196 Hz), with a dynamic measurement error less than 5% in the range of 0–800 Hz in the impact force test and a relative error within 5.5% in the sinusoidal excitation test. Moreover, a linearity of 0.2% is also achieved over the full scale range of the measuring platform.

1. Introduction

With the continuing advancement of deep space exploration, the performance requirements in terms of resolution, stability and accuracy for spacecraft with high stability such as large space telescopes keep increasing. The Chinese Space Station Telescope (CSST), for example, has been demonstrated to be able to calibrate GU wavelengths to an accuracy of a few kilometers per second and GV and GI to a few kilometers per second [1]. Moreover, the CSST aims to perform the high-spatial-resolution (~0.15″) imaging of targets that cover a large area of the sky (~17,500 deg^2) and wide wavelength range [2]. However, even small vibrations can affect the accuracy of such sophisticated equipment and it is therefore necessary to assess the impact of the forces generated by the vibration sources on the ground, which means that a high precision disturbance force measurement device is required. Additionally, the moving parts on the CSST have become larger; for example, the control moment gyroscope (CMG) has an output of 500 N·m and its mass is 90 kg, and a group of six control moment gyroscopes is typically used in a large space telescope [3]. With the addition of the mounting equipment, the measuring device is usually required to bear loads greater than one tonne in micro-vibration ground tests [4,5]. Additionally, each function module has a diameter of around 2 m. According to the above requirements, the measuring platform is required to have a good performance in terms of load capacity, mounting surface dimension, measurement accuracy, etc. In addition, the platform is expected to have a good stiffness (fundamental frequency) as the measurement objects are dynamic disturbance forces.

It is a fact that deformation based force measurement devices [6–16] (using strain gauges, capacitors, or piezometers etc.) do not have good performance in terms of load capacity and fundamental frequency in dynamic measurements with heavy loads, and some of which are also highly susceptible to the effects of temperature. However, piezoelectric measuring devices [17–20], which offer higher load capacity and greater robustness, can perform well when measuring in dynamics, hence the majority of vibration source measuring devices on the ground use piezoelectric systems. In previous studies of piezoelectric measuring devices, Stewart platforms have been widely used [21], but their loose structure reduces the stiffness of the platform [3], which limits the use of the device for heavy load measuring. In addition, the Stewart platform suffers from the disadvantages of over-constrained instability, difficult installation and high machining cost. Other measuring devices use more orthogonal distributions. Li [22], for example, described a piezoelectric six dimensional force measuring device for heavy loads that used a four-point support arrangement with a similar principle to the

* Corresponding author.
** Corresponding author at: Changchun Institute of Optics, Fine Mechanics and Physics, Chinese Academy of Science, Jilin, Changchun 130033, China.
E-mail addresses: xiamingyi@ciomp.ac.cn (M. Xia), xuzhenbang@ciomp.ac.cn (Z. Xu).

https://doi.org/10.1016/j.sna.2022.114085
Received 18 September 2022; Accepted 7 December 2022
Available online 9 December 2022

Kistler-type platform which is commercially available. However, this system is mainly used for static measurements of heavy loads and do not take into account the effects of structural coupling. Xia [3] proposed an eight-point supported (four points on the horizontal surface and four points on the vertical surface) dynamic disturbance force measuring platform which is still fundamentally a four-point support structure. In addition, Li [17,23] designed a five-point support load-sharing sensor. The load sharing ring was reasonably designed to effectively improve the load capacity of the measuring device, but it is mainly used at the end of robotic arms. Besides, Liu [24] designed an eight-point parallel-supported sensor, for which a mathematical model was derived, but redundant measurements inevitably introduced systematic errors (also occurred in article of Xia [3]) and it is difficult to ensure that the prototype is consistent with the measure principle well. Xia [25] proposed a sensor array measurement platform capable of measuring dynamic forces with significantly higher load capacity and fundamental frequency, but the platform is only capable of measuring three dimensional forces. The measuring platform therefore uses the similar parallel construction. Based on the above, existing measurement systems can hardly meet these requirements.

There are different measuring methods and structural designs for different measuring devices, according to the operating environment and testing conditions, and often one requirement needs to be met. However, high accuracy, good load capability and high stiffness measurement requirements can easily lead to conflicting designs, which are reflected in the followings. (1) When using conventional structures, increasing the size of the platform will reduce its stiffness and load capability. (2) The number of sensors connected in parallel will invariably be increased in order to achieve load sharing. When traditional measurement strategies are used, unacceptable errors can be introduced due to redundant decoupling. Therefore, this paper presents a measuring platform with a matrix of sensors and its novel measuring strategy. The basic structure of the platform is described in Section 2, which will greatly increase the upper limit of the platform dimension and load capacity through the use of sensor matrix and the addition of parallel links. Moreover, the relationship between redundant sensors and measurement errors is depicted. Section 3 selects the appropriate sensors for the measurement from the redundant sensors based on the D optimization with generalized inverse method and establishes decoupled expressions with higher accuracy. Section 4 describes experiments conducted for the pre-vibration and the evaluation of the dynamic mechanical characteristics of the platform.

2. Structure design and analysis

The measuring systems is shown in Fig. 1: a load platform, a base and sensors linking the two. In order to meet the measurement requirements, high demands are imposed on the platform dimension, load capacity, structural rigidity and accuracy of the measuring system. In the principle of measurement, these indicators often interact with each other. A novel platform is thus designed on the basis of the conventional system in terms of structure and measurement strategy.

2.1. Basic structure

Fig. 2 illustrates the basic structure and the working principle of the measuring platform. The addition of parallel sensors on the bottom and four sides of the load platform increases the dimension of the mounting surface, the load capacity and the rigidity of the measuring platform. Before measuring, the platform is mounted on the isolation platform via the base and the vibration source is installed on the load platform. Once the vibration source starts to operate, the dynamic forces/moments are delivered to the sensors and the disturbance forces/moments of the source can be obtained by calculating the output signals. Considering the ability to measure six dimensional forces/moments, the prototype in this paper has 4×4 sensors arranged in parallel on the bottom surface of the load platform and 2 sensors arranged vertically on each of the four sides of the load platform, where the parameters of the sensors are shown in Table 1, No. 1. The number and arrangement of redundant sensors are intended to increase the load capacity, the mounting surface dimension of the platform and the fundamental frequency of the platform and leave enough options for subsequent D optimization. However, the choice of the number and arrangement of sensors is not unique, as long as it meets the measurement requirements and is suitable for the application. The load capacity of the platform is primarily decided by the sensors (the simulation shows that the other components have little effect on the load capacity of the platform), which can achieve a maximum load of 520 kN (26 kN$\times$16 +26 kN$\times$0.5 $\times$8 =520 kN, where 0.5 is the tangential load factor).

The stiffness design of the platform using finite element analysis (FEA) is primarily analyzed as the load resolution and capacity of the platform is determined primarily by the sensors. As a test prototype, the base and load platform are made of metal sheet with comparatively low rigidity in order to leave room for performance improvement, where the size of the load platform is $350 \times 350 \times 15$ mm and the material is 7A09. For FEA models, a 1/8 symmetric modeling approach based on MSC Patran was used, as shown in Fig. 3(a). The element type of Hex 8 which has better computational accuracy was mainly used, and the nodes number was 18272, the elements number was 11578. Node coupling was used to attach these parts. Simulation results show that the platform has a fundamental frequency of 2296.8 Hz and a second order frequency of 2313.2 Hz, these frequencies are not in the range of interest (8–800 Hz) and cause very little structure coupling.

The simulation for platform of the same dimension with 2×2 sensors was also carried out as shown in Fig. 3(b). The fundamental and second order frequencies can be obtained as 636.1 Hz and 677.7 Hz respectively. Further, the simulations for two platforms with different mass loads were also performed as shown in Fig. 4, including the proposed platform with a load platform material of 40Cr. The comparison shows that the fundamental frequency of redundant matrix distributed

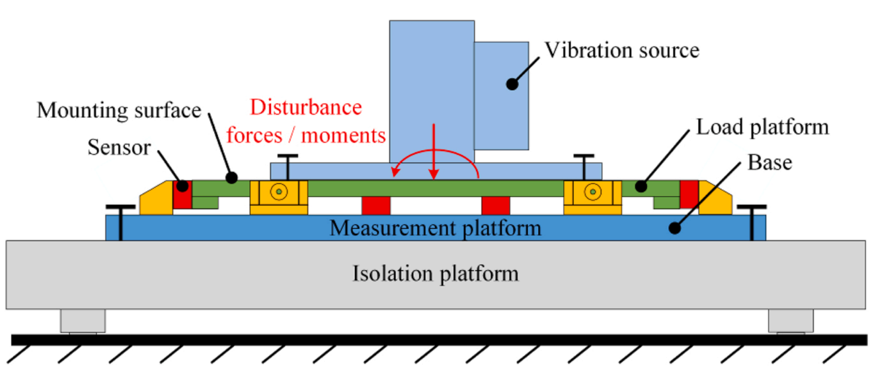

Fig. 1. Measuring system model.

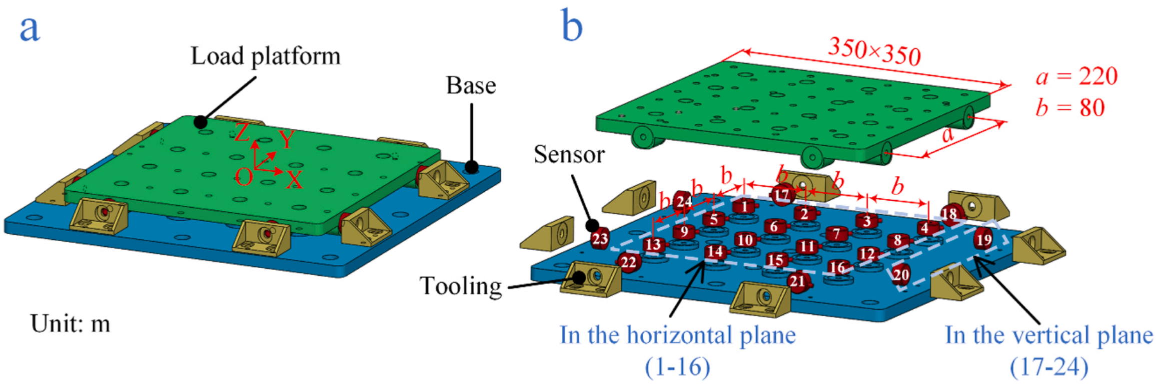

Fig. 2. The fundamental structure of the platform.

Table 1
Parameters of the sensors.

No.	Model	Sensitivity	Range	Preload	Resolution
1	9134B, Kistle	− 3.8 pC/N	26 kN	15–25 N·m	—
2	208C02, PCB	11.241 mV/N	±2224N-pk	—	0.004 N-rms

platform is increased compared to the platform with 2 × 2 sensors regardless of the load mass, which indicates a significant increase in the stiffness and loading capacity. Moreover, the new platform has a simpler structural design compared to conventional measurement equipment, and there are further improvements in performance by designing reinforcements for the load platform or changing its material.

2.2. Decoupled errors in redundant measuring

The improved stiffness and load capacity of the platform are benefits of adding sensors, but redundant sensors used can also have an impact on measurement accuracy due to system errors. The relevant theory has been investigated in the article [3], as shown in the following equation:

$$\zeta_a = 3\zeta_F + \zeta_V \tag{1}$$

where ζ_V, ζ_F and ζ_a are the relative error of the measurement output V, the error of the calibration force F and the error of the calibration of the sensor, respectively. If there are more calibration force vectors than six, the relative error of the calibration force matrix is magnified in comparison with its equivalent of six. This suggests that the redundant calibration causes the amplification of the systematic errors. However, there are many random components in the environmental error, so an appropriate increase in sensors participating can increase measurement

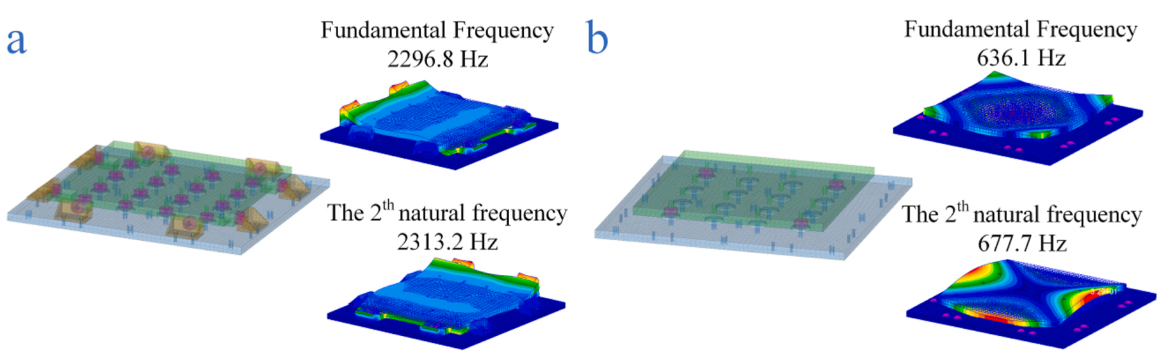

Fig. 3. Meshed models and fundamental frequencies of two platforms: (a) redundant sensors distributed platform; (b) platform with 2 × 2 sensors.

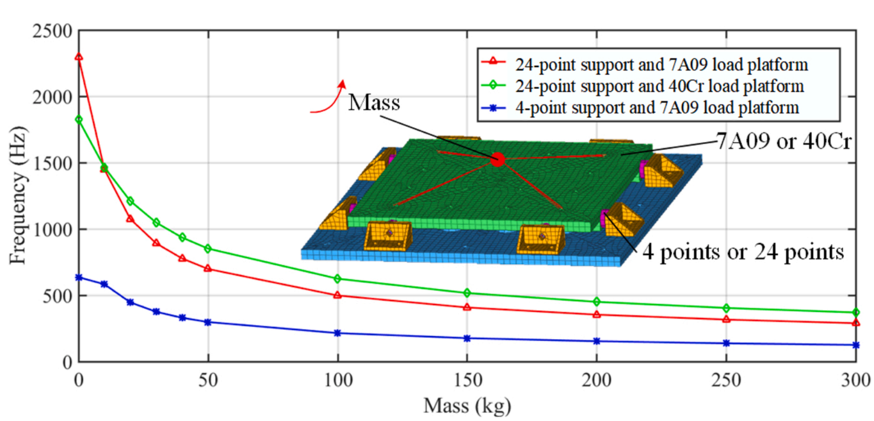

Fig. 4. Fundamental frequencies of two platforms with different mass loads.

accuracy when the environmental noise is high. Therefore an evaluation of the environmental noise needs to be carried out prior to the test and develop a measurement strategy.

Conventional measurement equipment cannot be optimized due to the system packaging, however it is possible to develop different measuring strategies for various sources of vibration on platform with redundant sensors. A method for choosing the suitable set of sensors is proposed to improve measurement accuracy while ensuring that the platform has the required structural characteristics in terms of mounting size, load capacity and stiffness.

3. Decoupling and its improvements

The sensitivity of the sensors in the platform cannot be accurately predicted, as environmental noise, vibration source characteristics, system processing and installation errors are all uncertainties in the measurement. When the loading tool was mounted at different locations on the platform and forces were input at its different positions, the responses of 24 sensors fitted by quadratic polynomials can be obtained as shown in Figs. 5–7. The figures include the time domain maximum values and the root mean square (RMS) in the frequency domain, which reflect transient response characteristics and the broadband response characteristics respectively, and these data have been normalized.

Fig. 5 contains the results when the load was input vertically at the centre of the platform. Theoretically, the response of these 16 sensors at the bottom (1−16) should be the same, however, the responses of these sensors are not consistent in practice due to the uncertainties mentioned above which is inevitable in actual tests. Fig. 6 shows the results with vertical input loads at the edge of the platform. It can be noticed that the response of sensors (1−16) far from the input is very weak, even approaching the ambient noise, a large measurement error will be generated if these sensors are used for decoupling. Fig. 7 illustrates the results with the horizontal input load. Sensors 17,18,21 and 22 have different statistics (which should be consistent) in Fig. 7(b) due to the above uncertainties.

Therefore the different vibration sources need to be assessed according the results of pre-vibration to construct different strategies for higher accuracy measurements. The problem can be categorized as follows: what is the number of sensors selected, which sensors to choose, and how to decouple.

3.1. Ambient noise assessment

First, an assessment of the ambient noise is required to decide how many sensors to select. A coherence function as shown in Eq. (2) is used to quantify the ambient noise.

$$\gamma^2 = \frac{|G_{fx}(\omega)|^2}{G_{ff}(\omega)G_{xx}(\omega)} \tag{2}$$

where $G_{fx}(\omega)$ is the mutual spectrum between the input and output signals, $G_{xx}(\omega)$ and $G_{ff}(\omega)$ are the self spectrum of the input signal and output signal respectively. The coherence function value satisfies the conditions of Eq. (3).

$$0 \le \gamma^2 \le 1 \tag{3}$$

When $\gamma^2 = 1$, it indicates that the signal is perfectly unaffected by the noise; when $\gamma^2 = 0$, it means that the signal is entirely drowned by the noise. In general, it is considered that the interference of environmental noise is small when $\gamma^2 > 0.8$, and the number of sensors m is chosen to be 6 as far as possible in order to introduce less systematic error. When $\gamma^2 < 0.8$, it is considered that the effect of environmental noise on the signals cannot be ignored and redundantly engaged sensors should be selected to reduce random errors.

3.2. Dynamic force decoupling

After that, the decoupling of dynamic forces is presented. The designed measuring platform is mainly used to measure the dynamic disturbance forces, and its calculation principle is thus based on spectrum analysis, as the time domain signal contains little dynamic information.

Assume that $U_i(t_k)$ and $F(t_k)$ are the output signals and the input signals in the time domain, where i denotes the i^{th} sensor channel. The corresponding frequency domain signals $U_i(\omega)$ and $F(\omega)$ can be obtained from Eq. (4) which is a discrete Fourier transform equation, where $x(t_k)$ is the signal in the time domain and $X(\omega_n)$ is the signal in the frequency domain.

$$X(\omega_n) = \mathrm{DFT}\left\{x(t_k)\right\} = \sum_{k=0}^{N-1} x(t_k)e^{-j2\pi kn/N} \tag{4}$$

Decoupling of six dimensional forces can be then performed by arbitrarily selecting the output signals of m sensors. The generalized inverse based decoupling algorithm is chosen for the selection of the optimal combination of output channels, taking into account the savings of computer resources and the advantages of Matlab in the resolution of matric.

The $\mathbf{F}(\omega) = [F_x(\omega)\ F_y(\omega)\ F_z(\omega)\ M_x(\omega)\ M_y(\omega)\ M_z(\omega)]^{\mathrm{T}}$ indicates the input dynamic disturbance forces, $\mathbf{U}(\omega) = [U_1(\omega)\ U_2(\omega)\ \ldots\ U_m(\omega)]^{\mathrm{T}}$ is the voltage output signals from m sensors, then the relationship between the input and output can be expressed as Eq. (5).

$$\begin{bmatrix} U1(\omega) \\ U2(\omega) \\ U3(\omega) \\ \vdots \\ Um(\omega) \end{bmatrix} = \begin{bmatrix} V11(\omega) & \cdots & V61(\omega) \\ V12(\omega) & \cdots & V62(\omega) \\ V13(\omega) & \cdots & V63(\omega) \\ \vdots & \ddots & \vdots \\ V1m(\omega) & \cdots & V6m(\omega) \end{bmatrix} \begin{bmatrix} F_x(\omega) \\ F_y(\omega) \\ F_z(\omega) \\ M_x(\omega) \\ M_y(\omega) \\ M_z(\omega) \end{bmatrix} + \mathbf{B}(\omega) \tag{5}$$

where $\mathbf{B}(\omega)$ is the error matrix, and the Eq. (6) can be obtained from Eq. (5).

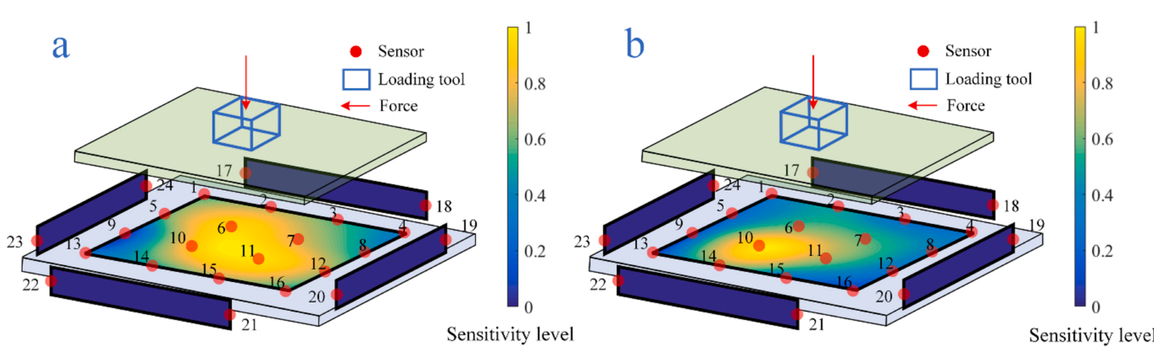

Fig. 5. Response of the sensors when subjected to F_z: (a) maximum value in the time domain; (b) RMS in the frequency domain.

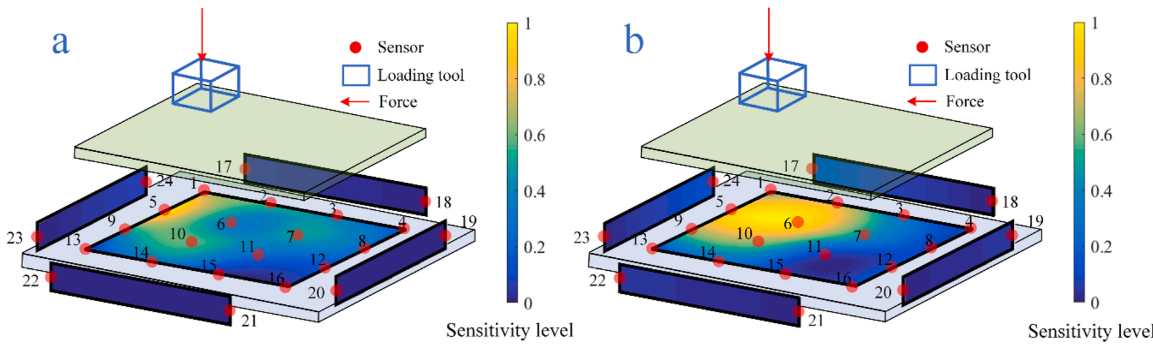

Fig. 6. Response of the sensors when subjected to M_x, M_y and F_z: (a) maximum value; (b) RMS.

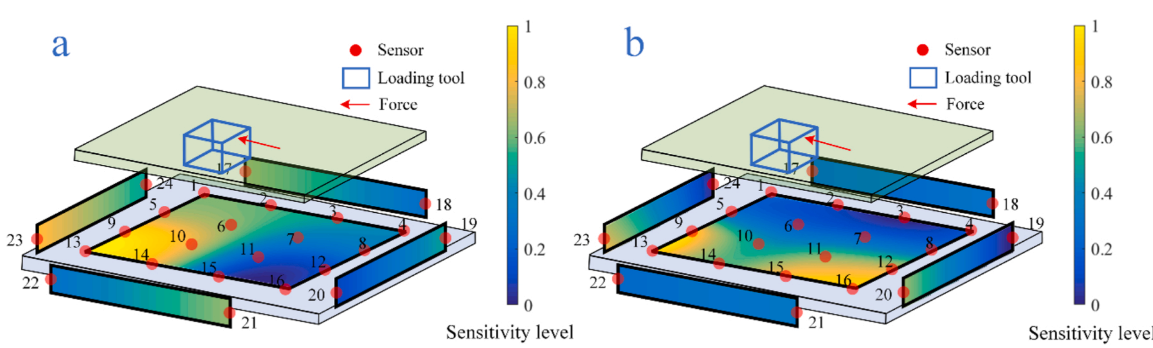

Fig. 7. Response of the sensors when subjected to F_x, M_y and M_z: (a) maximum value; (b) RMS.

$$\mathbf{U}(\omega) = \mathbf{V}(\omega)\mathbf{F}(\omega) + \mathbf{B}(\omega) \tag{6}$$

In order to make indicator $J = \mathbf{B}(\omega)^{\mathrm{T}}\mathbf{B}(\omega)$ minimal, $\mathbf{V}(\omega)$ can be accessed by the generalized inverse of the matrix as shown in Eq. (7).

$$\mathbf{V}(\omega) = \mathbf{U}(\omega)\mathbf{F}(\omega)^{\mathrm{T}}\left(\mathbf{F}(\omega)\mathbf{F}(\omega)^{\mathrm{T}}\right)^{-1} \tag{7}$$

By substituting the above equation into Eq. (6), the least squares estimate of $\mathbf{F}(\omega)$ is calculated:

$$\mathbf{F}'(\omega) = \left(\mathbf{V}(\omega)^{\mathrm{T}}\mathbf{V}(\omega)\right)^{-1}\mathbf{V}(\omega)^{\mathrm{T}}\mathbf{U}(\omega) \tag{8}$$

The accuracy of the estimated input disturbance force $\mathbf{F}'(\omega)$ depends on the selection of m output voltages from 24 output channels.

3.3. 3.3 Optimization algorithm

Which m of the 24 sensors will be selected as the optimal sensor set for the above calculation is discussed below. $\mathbf{U}_{cs}(\omega)$ denotes the 24 measured output voltages from 24 sensors which is called the candidate set, and m output voltages are selected from the candidate set to form $\mathbf{U}(\omega)$. We use D optimization [26–28] to select the optimal $\mathbf{U}(\omega)$.

Assuming that the measurement errors are independent statistically with a standard deviation of σ, $var[\mathbf{F}'(\omega)] = \sigma^2[\mathbf{V}^{\mathrm{T}}(\omega)\mathbf{V}(\omega)]^{-1}$, where σ^2 is a constant and $[\mathbf{V}^{\mathrm{T}}(\omega)\mathbf{V}(\omega)]^{-1}$ is the sensitivity of $\mathbf{F}'(\omega)$; lower sensitivity corresponds to higher accuracy of $\mathbf{F}'(\omega)$ [26]. Therefore, choosing the m output voltages that maximize the value of $|\mathbf{V}^{\mathrm{T}}(\omega)\mathbf{V}(\omega)|$ gives the most accurate $\mathbf{F}'(\omega)$, which is called D optimal design, where D refers to the determinant, and the optimal output voltage $\mathbf{U}(\omega)$ can be obtained using the sequential exchange method [29].

The m sensors ($\mathbf{U}(\omega)$) are selected from the 24 sensors ($\mathbf{U}_{cs}(\omega)$) randomly, but ensuring that $\mathbf{U}(\omega)$ selected can be used to fully decouple the six dimensional forces/moments. $\mathbf{V}(\omega)$ is initialized by substituting the output data into Eq. (7). Then select a sensor from the remaining sensors and remove the one sensor from the $m+1$ sensors, ensuring that m sensors after deletion make $[\mathbf{V}^{\mathrm{T}}(\omega)\mathbf{V}(\omega)]$ maximum. The selection and deletion of sensors does not stop until the value of $[\mathbf{V}^{\mathrm{T}}(\omega)\mathbf{V}(\omega)]$ is not further improved. The final $\mathbf{U}(\omega)$ is the optimal result $\mathbf{U}_{\mathrm{opt}}(\omega)$, the optimal combination of sensors can also be obtained.

The process of D optimization is shown in Fig. 8.

3.4. Improved decoupling

Despite the advantages of the generalized inverse based decoupling method in terms of computer processing speed, this method does not consider the case when the matrix of voltage is zero and is prone to ill-conditioning matrices when the calibration errors are large, which can easily reduce the accuracy of the measurement. Therefore, the decoupling method in the previous subsection can be used to find the optimal set of sensors, but the corresponding output signals require more accurate six dimensional force decoupling operations. The full regression linear decoupling algorithm is introduced.

The decoupling of force $F_z(\omega)$ is first analyzed. Let $U_{1k}(\omega)$, $U_{2k}(\omega)$,…, $U_{nk}(\omega)$ ($n = 1, 2,…, m$; $k = 1, 2,…, h$) be optimal sensors output data, where $U_{nk}(\omega)$ indicates the n^{th} optimal sensor output at the k^{th} force input point. Of course, the measured inputs also have h sets. The relation between $F_z(\omega)$ and the $U_n(\omega)$ is shown in Eq. (9) as a polynomial formulation using the regression method.

$$F_z(\omega) = \beta_0(\omega) + \beta_1(\omega)U_1(\omega) + \beta_2(\omega)U_2(\omega) + \cdots + \beta_m(\omega)U_m(\omega) + \varepsilon(\omega) \tag{9}$$

where $\varepsilon(\omega)$ is the residual error and $\beta_i(\omega)$ ($i = 0,1,2, …,m$) are the regression coefficients. Calculating the h sets of data gives the regression coefficients from the pre-vibration test. Eq. (10) can be obtained when the test data are substituted into Eq. (9).

$$F_{zk}(\omega) = \beta_0(\omega) + \beta_1(\omega)U_{1k}(\omega) + \beta_2(\omega)U_{2k}(\omega) + \cdots + \beta_m(\omega)U_{mk}(\omega) + \varepsilon_k(\omega) \tag{10}$$

Let the the $\varepsilon_k(\omega)$ be $e_k(\omega)$ and $\beta_i(\omega)$ be $b_i(\omega)$. Eq. (10) can be reformulated as Eq. (11).

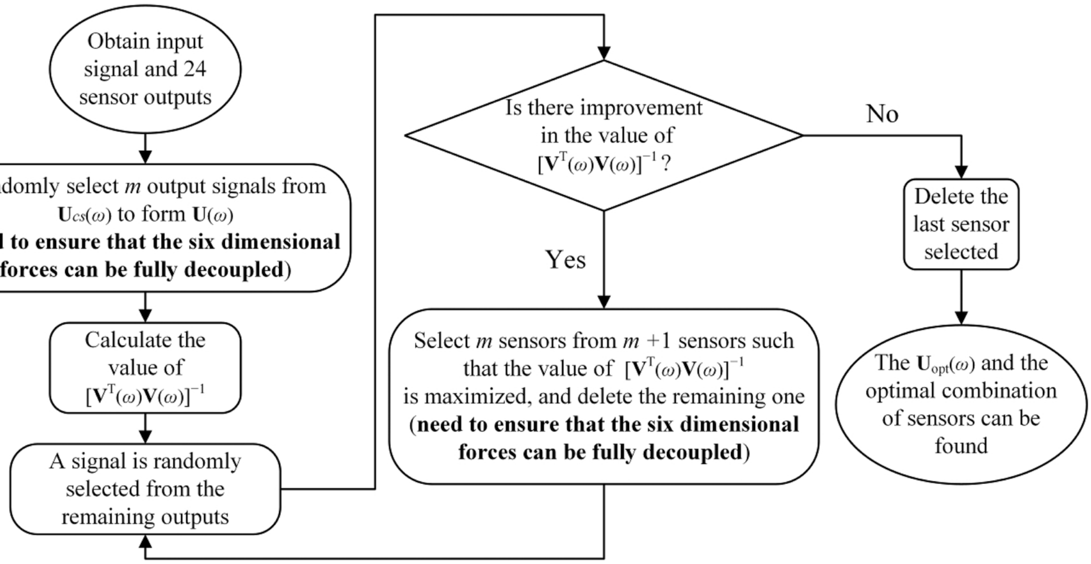

Fig. 8. The process of D optimization.

$$F_{zk}(\omega) = b_0(\omega) + b_1(\omega)U_{1k}(\omega) + b_2(\omega)U_{2k}(\omega) + \cdots + b_m(\omega)U_{mk}(\omega) + e_k(\omega) \tag{11}$$

If $e_k(\omega)$ is ignored, then the estimate of $F_{zk}(\omega)$ is $\widehat{F}_{zk}(\omega)$, whose expression is shown in Eq. (12).

$$\widehat{F}_{zk}(\omega) = b_0(\omega) + b_1(\omega)U_{1k}(\omega) + b_2(\omega)U_{2k}(\omega) + \cdots + b_m(\omega)U_{mk}(\omega) \tag{12}$$

The $e_k(\omega)$ can be obtained by combining the Eq. (11) and Eq. (12):

$$\begin{gathered} e_k(\omega) = F_{zk}(\omega) - \widehat{F}_{zk}(\omega) \\ = F_{zk}(\omega) - (b_0(\omega) + b_1(\omega)U_{1k}(\omega) + b_2(\omega)U_{2k}(\omega) + \cdots + b_m(\omega)U_{mk}(\omega)) \end{gathered} \tag{13}$$

By minimizing the sum of squares of residuals $e_k(\omega)$, $b_i(\omega)$ can be calculated:

$$Q = \sum_{k=1}^{h} e_k{}^2(\omega) = \sum_{k=1}^{h} [F_{zk}(\omega) - \widehat{F}_{zk}(\omega)]^2 \tag{14}$$

In order to minimize Q, Eq. (15) can be obtained from the extreme value principle.

$$\frac{\partial Q}{\partial b_n(\omega)} = 0\left(n = 1, 2, \ldots, m\right) \tag{15}$$

Expanding the above equation gives Eq. (16):

$$\sum_{k=1}^{h}[F_{zk}(\omega) - (b_0(\omega) + b_1(\omega)U_{1k}(\omega) + b_2(\omega)U_{2k}(\omega) + \cdots + b_m(\omega)U_{mk}(\omega))] = 0 \tag{16}$$

The data from each test are averaged as shown in Eq. (17) and Eq. (18).

$$\overline{U}_n(\omega) = \frac{1}{h}\sum_{k=1}^{h} U_{nk}(\omega)\left(n = 1, 2, \ldots, m\right) \tag{17}$$

$$\overline{F}_z(\omega) = \frac{1}{h}\sum_{k=1}^{h} F_{zk}(\omega) \tag{18}$$

Substituting Eqs. (17) and (18) to Eq.(14) yields b_0::

$$b_0(\omega) = \overline{F}_z - \sum_{n=1}^{m} b_n(\omega)\overline{U}_n(\omega) \tag{19}$$

Writing the variables $U_{nk}(\omega)$ and $F_{zk}(\omega)$ in the form of deviations from the mean of the measured data makes it easier to calculate Eq. (19):

$$U'_{nk} = U_{nk}(\omega) - \overline{U}_n(\omega) \tag{20}$$

$$F'_{zk} = F_{zk}(\omega) - \overline{F}_z(\omega) \tag{21}$$

Eqs. (20) and (21) are then substituted into Eqs. (12) - (14) to obtain Eqs. (22) - (24).

$$\widehat{F}_{zk}(\omega) = \overline{F}_z + \left[b_1(\omega)U'_{1k}(\omega) + b_2(\omega)U'_{2k}(\omega) + \cdots + b_m(\omega)U'_{mk}(\omega)\right] \tag{22}$$

$$\begin{gathered} e_k(\omega) = F_{zk}(\omega) - \widehat{F}_{zk}(\omega) \\ = F'_{zk} - \left[b_1(\omega)U'_{1k}(\omega) + b_2(\omega)U'_{2k}(\omega) + \cdots + b_m(\omega)U'_{mk}(\omega)\right] \end{gathered} \tag{23}$$

$$Q = \sum_{k=1}^{h} e_k{}^2(\omega) \tag{24}$$

Eq. (15) can be written as Eq. (25):

$$\begin{gathered} -\frac{\partial Q}{2\partial b1} = \sum_{k=1}^{h}\left[F'_{zk}(\omega) - \left(b_1(\omega)U'_{1k}(\omega) + \cdots + b_m(\omega)U'_{mk}(\omega)\right)\right]U'_{1k}(\omega) = 0 \\ -\frac{\partial Q}{2\partial b2} = \sum_{k=1}^{h}\left[F'_{zk}(\omega) - \left(b_1(\omega)U'_{1k}(\omega) + \cdots + b_m(\omega)U'_{mk}(\omega)\right)\right]U'_{2k}(\omega) = 0 \\ \vdots \\ -\frac{\partial Q}{2\partial bm} = \sum_{k=1}^{h}\left[F'_{zk}(\omega) - \left(b_1(\omega)U'_{1k}(\omega) + \cdots + b_m(\omega)U'_{mk}(\omega)\right)\right]U'_{mk}(\omega) = 0 \end{gathered} \tag{25}$$

Eq. (25) is rewritten as Eq. (26) in matrix form:

$$\begin{bmatrix} b1(\omega) \\ b2(\omega) \\ \vdots \\ bm(\omega) \end{bmatrix}^{T} \begin{bmatrix} S11(\omega) & S21(\omega) & \cdots & Sm1(\omega) \\ S12(\omega) & S22(\omega) & \cdots & Sm2(\omega) \\ \vdots & \vdots & \ddots & \vdots \\ S1m(\omega) & S2m(\omega) & \cdots & Smm(\omega) \end{bmatrix} = \begin{bmatrix} S1y(\omega) \\ S2y(\omega) \\ \vdots \\ Smy(\omega) \end{bmatrix}^{T} \tag{26}$$

where $Sij(\omega) = \sum_{k=1}^{h} U'_{ik}(\omega)U'_{jk}(\omega)$, $Siy(\omega) = \sum_{k=1}^{h} F'_{zk}(\omega)U'_{ik}(\omega)$.

From the calculation above, the regression expression of Eq. (12) is derived. In the same way, force regression equations in other directions can be obtained. With the previous analysis, the sensors used for the measurements can be obtained and the six-dimensional forces can be decoupled.

4. Experiment

On the basis of the design and analysis mentioned above, a prototype of the measuring platform was manufactured. After the verification of the linearity and the rigidity of the platform, pre-vibration experiments were conducted to select the optimal combination of sensors. Then the dynamic mechanical characteristics of the platform were investigated, verifying the validity of the above theory.

4.1. Testing for the performance of platform

Fig. 9 shows the test system comprising calibration equipment (homemade, the parameters of the force sensors used in the equipment are shown in Table 1, No. 2), loading tool, a data acquisition device (VRAI820–24 bit, M+P, Germany; precision: $\pm$ 0.1 dB), charge amplifier (CT5853, gain: 0.01–1000, precision: 1%) and PC.

Good linearity is the foundation of a dynamic measuring platform and this was verified preliminarily by the measurements of the frequency response function (FRF) curves for sensors. The calibration equipment was used to input three forces of different magnitudes under the same incentive mode to the loading tool, where the FRF curves of sensors 4 is shown in Fig. 10. The fundamental frequency of the redundant matrix distributed platform can be obtained as 2196 Hz with a acquisition frequency of 8192 Hz and a acquisition time of 16 s (the sample coefficient is 2.56, and the bandwidth is 1/16–3200 Hz). This is very similar to the simulation result of 2296.8 Hz, which illustrates the simple structural design of this platform and the simulation results can provide good guidance for the design. Furthermore, it is easy to improve the stiffness of the platform by strengthening the load platform and the base as mentioned previously.

Using an input force of 334.1 N as a reference, the relative errors of input pulses of 100.3 and 408.7 N for sensor 4 are presented in Table 2, showing an average relative error within 4% (dynamic linearity within 0.2%FS). This approach is intended to describe the linearity of individual output in a wide-band and does not fully reflect the linearity of the six-dimensional forces of the novel platform after the calibration.

4.2. Pre-vibration experiment

Positions 1–6 of the load platform was installed with the loading tool as shown in Fig. 11(c). There are 21 points of loading on the loading tool and impact forces can be input to the loading tool as shown in Fig. 11 (a) using the calibration equipment.

This experiment chose points 1, 9, 10, 13, 16 and 19 and three broadband force impacts were applied to each point. In order to reduce the effect of random errors, the three measurements of the signals from the sensors of the calibration equipment and the 24 output sensors were averaged as input data and measured data. The data of input and output can be obtained with a acquisition frequency of 2048 Hz and a acquisition time of 16 s

Substituting the data obtained into Eq.(2) revealed that the environment interferes slightly with the signals, therefore the number of sensors was chosen to be 6.

The data in the frequency domain was obtained by substituting the six sets of experimental time domain data into Eq. (4). Note that the input forces here need to be converted to the forces/moments operating at the center of the loading platform O using Eq. (27).

$$\mathbf{F}(\omega)=\mathbf{C}\begin{bmatrix} Fin-1(\omega) & 0 & 0 & 0 & 0 & 0 \\ 0 & Fin-9(\omega) & 0 & 0 & 0 & 0 \\ 0 & 0 & Fin-10(\omega) & 0 & 0 & 0 \\ 0 & 0 & 0 & Fin-13(\omega) & 0 & 0 \\ 0 & 0 & 0 & 0 & Fin-16(\omega) & 0 \\ 0 & 0 & 0 & 0 & 0 & Fin-19(\omega) \end{bmatrix} \tag{27}$$

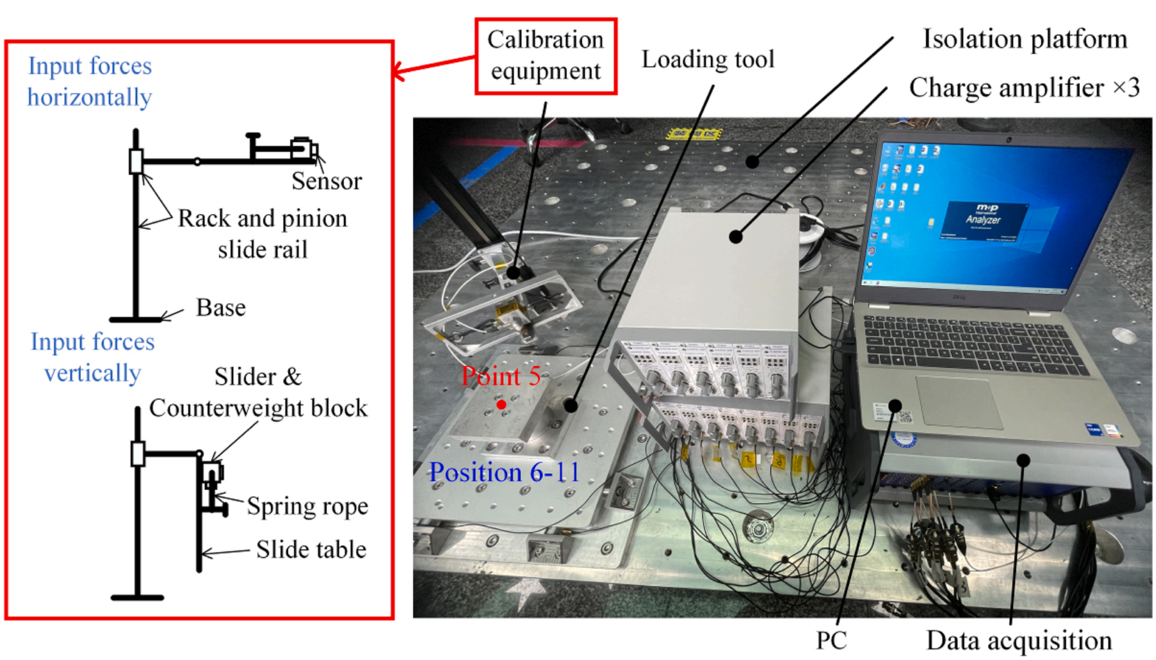

Fig. 9. Test system.

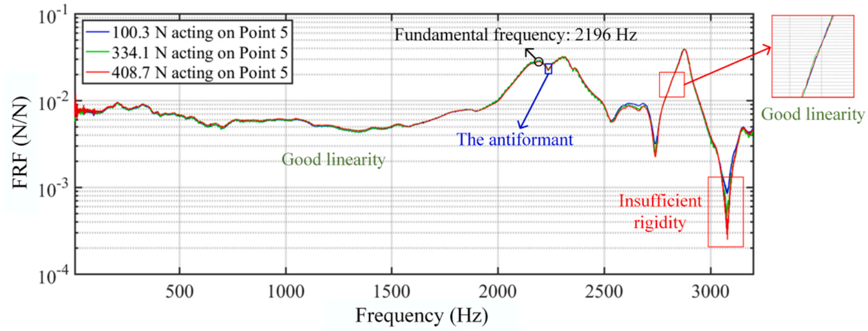

Fig. 10. FRF curves of the platform.

Table 2
Relative error of the transfer function for different amplitude impulses.

Frequency range (Hz)	Relative error (%)	
	100.3 N	408.7 N
1–800	3.4	2.9
800–1600	2.8	3.7
1600–2400	3.2	3.1
2400–3200	5.7	4.8

where **C** is given by Eq. (28) which can be obtained from Fig. 11, and $F_{\text{in-}i}$ is the input force acting at point i.

$$\mathbf{C} = \begin{bmatrix} 0 & 0 & 0 & -1 & 0 & 1 \\ 0 & 0 & -1 & 0 & 1 & 0 \\ -1 & -1 & 0 & 0 & 0 & 0 \\ -0.15 & -0.05 & 0.075 & 0 & -0.075 & 0 \\ -0.15 & -0.05 & 0 & -0.075 & 0 & 0.075 \\ 0 & 0 & 0.15 & 0.15 & -0.05 & -0.05 \end{bmatrix} \tag{28}$$

Rewriting Eq. (5) gives Eq. (29):

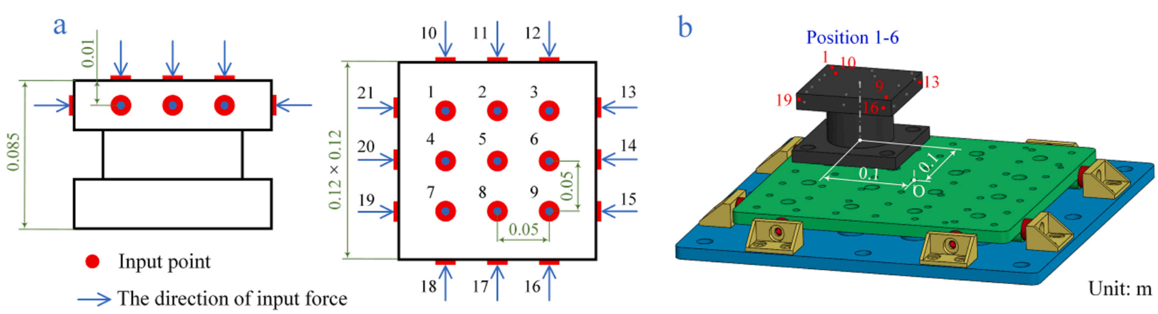

Fig. 11. Input points on the loading tool: (a) schematic of the loading tool and its input points; (b) platform with tool.

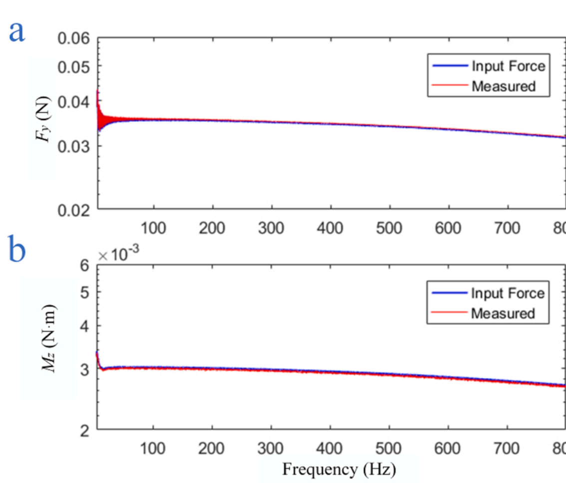

Fig. 12. Comparison of input impact forces with measured forces using 6 sensors and D optimization:(a) F_y; (b) M_z.

$$\begin{bmatrix} U11(\omega) & U19(\omega) & U110(\omega) & U113(\omega) & U116(\omega) & U119(\omega) \\ U21(\omega) & \ddots & & & & \vdots \\ U31(\omega) & & \ddots & & & \vdots \\ U41(\omega) & & & \ddots & & \vdots \\ U51(\omega) & & & & \ddots & \vdots \\ U61(\omega) & \cdots & \cdots & \cdots & \cdots & U619(\omega) \end{bmatrix} = \begin{bmatrix} V11(\omega) & V12(\omega) & V13(\omega) & V14(\omega) & V15(\omega) & V16(\omega) \\ V12(\omega) & \ddots & & & & \vdots \\ V13(\omega) & & \ddots & & & \vdots \\ V14(\omega) & & & \ddots & & \vdots \\ V15(\omega) & & & & \ddots & \vdots \\ V61(\omega) & \cdots & \cdots & \cdots & \cdots & V66(\omega) \end{bmatrix} \mathbf{F}(\omega) + \mathbf{B}(\omega) \tag{29}$$

where $U_{i1}(\omega)$, $U_{i9}(\omega)$, $U_{i10}(\omega)$ $U_{i13}(\omega)$, $U_{i16}(\omega)$, $U_{i19}(\omega)$ $(i = 1,2,\ldots,6)$ denote the outputs of six sensors selected arbitrarily.

Deriving Eq. (29), the calibration matrix $\mathbf{V}(\omega)$ is obtained for an arbitrary selection of six sensors, these six sensors were used as the initial combination of sensors and D optimization was performed. The optimal combination of six sensors can be obtained with the D optimization. And sensors 1, 5, 6, 17, 21 and 24 were selected as the optimal sensors. Subsequently, the output signals of these 6 sensors were linearly decoupled using a full regression based method to obtain the more accurate decoupling expressions.

4.3. Dynamic precision test

Initially, based on the optimal sensor combination and decoupling expressions obtained from the above pre-vibration experiments, impact forces were applied to point 11 of the loading tool and the impact forces were measured to verify the dynamic accuracy of the platform. The energy of a impulse signal can cover a wide frequency bandwidth, so the impact forces are suitable for verifying accuracy over the entire bandwidth of interest.

Fig. 12 shows comparisons of the input impact forces and the measured forces using 6 sensors and D optimization, where (a) is the comparison for F_y and (b) is the comparison for M_z.

From Eq. (30), the dynamic errors in the measurement of the forces can be obtained as shown in Table 3.

$$\xi_i(\omega_j) = \frac{|F_{\mathrm{obi}}(\omega_j)| - |F_i(\omega_j)|}{|F_i(\omega_j)|} \times 100\%, \left(i = 1,2; j = 1,2\cdots n_{\mathrm{fft}}\right) \tag{30}$$

where i represents the two impact forces, and j indicates different frequencies. The dynamic relative errors are within 5% in the range of 8–800.

Compared to the measurement curve of a conventional measurement platform [3] as shown in Fig. 13(a), the proposed platform has a higher measurement accuracy and does not suffer from distortion of the calibration matrix as the frequency increases (as shown in the green box) due to its significantly higher stiffness compared to systems of the same size. In addition, measurements with and without D optimization are compared. It can be found in Fig. 13(b) that D optimization selects the sensors with higher signal quality and less interference from the environmental noisy which improves the accuracy of the measurement. If the measurement environment is significantly noisy, the effect of D optimization will be even more pronounced. This is exactly the advantage of the platform with redundant sensors, which is absent in conventional systems. It has also been verified by comparing the green and red curves in Fig. 13(b) that redundant sensors can cause greater errors when the ambient noise is low.

Finally, as a practical application, multi-frequency sinusoidal excitation generated by a six dimensional simulator (relative error: within 3.33%) [30] was measured to further test the accuracy of the platform. The test system with simulator is shown in Fig. 14, where the simulator was installed on the load platform and the target disturbance output of the simulator was controlled by closed loop. This simulator was fitted with a load allowing the simulator to provide higher accuracy in low frequency vibration. Similarly, to ensure the accuracy of the measurements, the pre-vibration experiments were re-implemented, the optimal combination of sensors were re-found and the decoupling expressions were re-obtained before the measurement.

Table 3
Dynamic errors in the range of 8–800 Hz.

Range (Hz)	Dynamic errors (%)	
	F_y	M_z
1–100	4.31	2.86
100–200	2.77	1.37
200–300	1.84	2.01
300–400	0.78	1.34
500–600	1.35	0.89
500–700	1.54	1.54
700–800	0.99	1.78

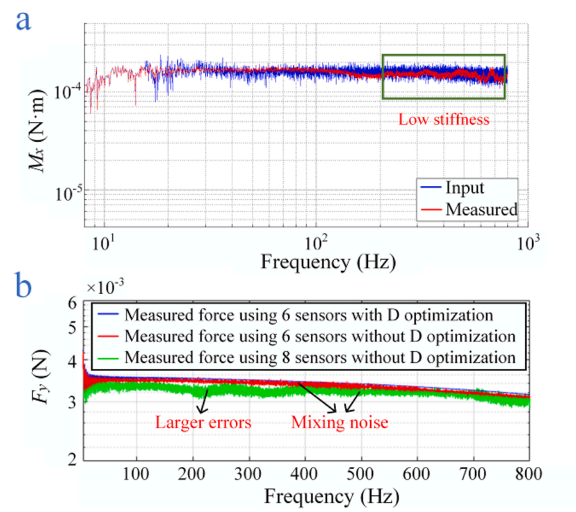

Fig. 13. Measurement curves from conventional system [3] and novel platform: (a) low stiffness of the traditional system [3]; (b) measured results with and without D optimization.

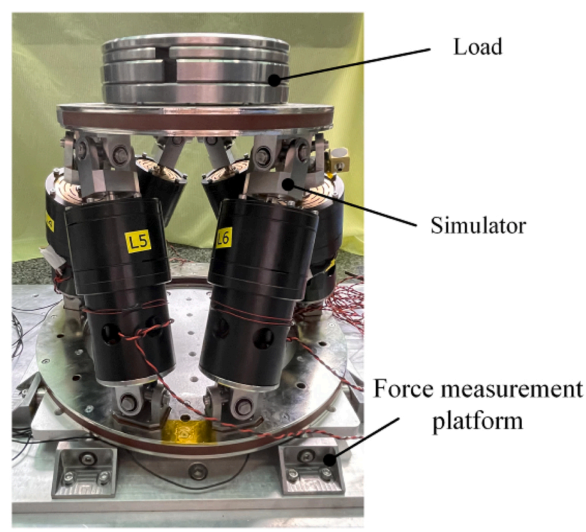

Fig. 14. Test system with simulator.

In the Fig. 15, the disturbance forces of the cryocooler (80 Hz, 160 Hz, 240 Hz) and CMG (46.7 Hz, 116.7 Hz, 233 Hz) were simulated. Besides, the 8 Hz is used to test the low frequency characteristics of the platform, and the frequencies corresponding to the peaks in all four graphs are the same as the seven frequencies above. The data in the Table 4 show that the dynamic measurement accuracy of the platform is within 5.5%, except for the poor measurement accuracy at 8 Hz, which is caused by the inferior low frequency dynamic performance of the piezo material.

5. Conclusions

This paper presents the design, analysis and test of a redundant matrix sensors based dynamic force measuring platform for large equipment in spacecraft. The platform adopts the matrix of sensors to improve the load capacity, mounting surface dimension and stiffness of the novel platform. Additionally, D optimization is introduced to select the optimal sensors and the full regression linear decoupling algorithm avoids the disadvantages of traditional decoupling methods which

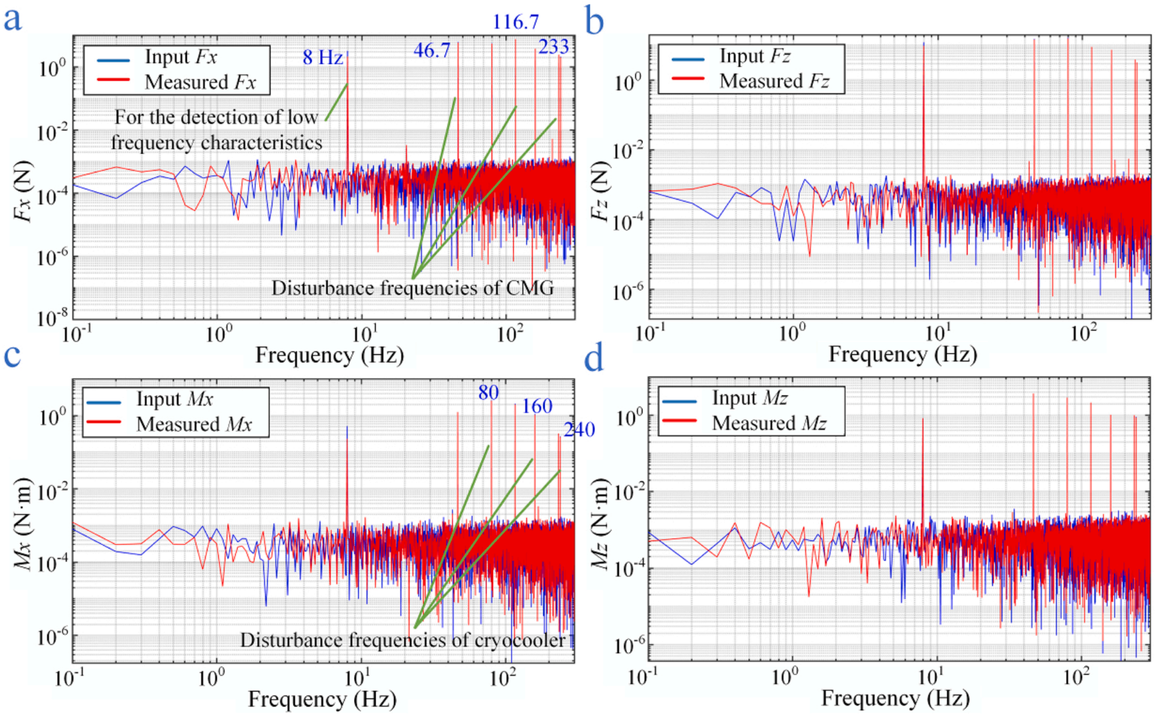

Fig. 15. Input force vs the measured force in the sinusoidal excitation test.

Table 4
Input force and the measured force in the sinusoidal excitation test.

Frequency		8 Hz	46.7 Hz	80 Hz	116.7 Hz	160 Hz	233 Hz	240 Hz
F_x (N)	Input	3.20	6.10	5.50	7.40	3.60	2.30	2.10
	Measured	2.12	5.83	5.38	7.42	3.73	2.41	1.99
F_z (N)	Input	12.10	15.30	16.50	8.60	7.10	3.80	3.10
	Measured	9.60	14.51	15.71	8.92	7.38	3.87	3.19
M_x (Nm)	Input	0.51	1.20	2.60	2.10	1.10	0.31	0.27
	Measured	0.23	1.24	2.52	1.99	1.05	0.32	0.26
M_z (Nm)	Input	0.69	3.51	2.82	2.01	0.95	0.91	0.90
	Measured	0.83	3.66	2.87	2.12	1.01	0.99	0.87

improves measurement accuracy.

Simulation and experiment indicate that the platform ensures a high stiffness and load capacity, where the platform has a fundamental frequency of 2196 Hz, a load capacity of 520 kN and a linearity of better than 0.2%FS. And the dynamic relative error of the six dimensional generalized forces/moments in force impact tests can be within 5% in the range of 8–800 Hz and within 5.5% in sinusoidal excitation experiments, verifying the applicability of the measuring platform in the ground testing of dynamic forces from vibration sources.

Funding

This work was supported by the National Natural Science Foundation of China (NO. 11672290).

Declaration of Competing Interest

The authors declare that they have no known competing financial interests or personal relationships that could have appeared to influence the work reported in this paper.

Data availability

The authors do not have permission to share data.

References

[1] H.B. Yuan, D.S. Deng, S. Yang, A star-based method for precise wavelength calibration of the Chinese Space Station Telescope (CSST) slitless spectroscopic survey, Res. Astron. Astrophys. 21. 3 (2021) 074, https://doi.org/10.1088/1674-4527/21/3/074.

[2] Y. Cao, Y. Gong, Z.Y. Zheng, et al., Calibrating photometric redshift measurements with the Multi-channel Imager (MCI) of the China Space Station Telescope (CSST), Res. Astron. Astrophys. 22 (2) (2022), 025019, https://doi.org/10.1088/1674-4527/ac424e.

[3] M.Y. Xia, Z.B. Xu, K. Han, Q. Huo, A. Li, Dynamic disturbance force measurement platform for large moving device in spacecraft, J. Sound Vib. 447 (2019) 61–77, https://doi.org/10.1016/j.jsv.2019.01.053.

[4] B.J. Kawak, Development of a low-cost, low micro-vibration CMG for small agile satellite applications, Acta Astronaut. 131 (2017) 113–122, https://doi.org/10.1016/j.actaastro.2016.10.021.

[5] L. Li, L. Tan, et al., The influence of flywheel micro vibration on space camera and vibration suppression, Mech. Syst. Signal Process. 100 (2018) 360–370, https://doi.org/10.1016/j.ymssp.2017.07.029.

[6] J.W. Guggenheim, et al., Robust and inexpensive six-axis force-torque sensors using MEMS barometers, IEEE/ASME Trans. Mechatron. 22. 2 (2017) 838–844, https://doi.org/10.1109/TMECH.2017.2654446.

[7] U. Kim, et al., A novel six-axis force/torque sensor for robotic applications, IEEE/ASME Trans. Mechatron. 22. 3 ((2016) 1381–1391, https://doi.org/10.1109/TMECH.2016.2640194.

[8] T. Liu, et al., Design of a three-dimensional capacitor-based six-axis force sensor for human-robot interaction, Sens. Actuators A: Phys. 331 (2021), 112939, https://doi.org/10.1016/j.sna.2021.112939.

[9] Z.J. Zhang, et al., A six-dimensional traction force sensor used for human-robot collaboration, Mechatronics 57 (2019) 164–172, https://doi.org/10.1016/j.mechatronics.2018.12.005.

[10] Ismael Payo, et al., Six-axis column-type force and moment sensor for robotic applications, IEEE Sens. J. 18. 17 ((2018) 6996–7004, https://doi.org/10.1109/JSEN.2018.2853561.
[11] L.P. Chao, and L.T. Chen. Shape optimal design and force sensitivity evaluation of six-axis force sensors. Sensors and Actuators A: Physical 63.2 (1997): 105–112. https://doi.org/10.1016/S0924–4247 (97)01534–3.
[12] Gab-Soon Kim, Design of a six-axis wrist force/moment sensor using FEM and its fabrication for an intelligent robot, Sens. Actuators A: Phys. 133. 1 (2007) 27–34, https://doi.org/10.1016/ j.sna.2006.03.038.
[13] Q.K. Liang, D. Zhang, Q.J. Song, et al., Design and fabrication of a six-dimensional wrist force/torque sensor based on E-type membranes compared to cross beams, Meas. 43. 10 (2010) 1702–1719, https://doi.org/10.1016/ j. measurement.2010.09.010.
[14] Y.J. Sun, et al., Design and optimization of a novel six-axis force/torque sensor for space robot, Measurement 65 (2015) 135–148, https://doi.org/10.1016/j. measurement.2015.01.005.
[15] K. Han, et al., Design and optimization of a high sensitivity joint torque sensor for robot fingers, Measurement 152 (2020), 107328, https://doi.org/10.1016/j. measurement.2019.107328.
[16] B. Wu, J. Luo, F. Shen, et al., Optimum design method of multi-axis force sensor integrated in humanoid robot foot system, Measurement 44 (9) (2011) 1651–1660, https://doi.org/10.1016/j. measurement.2011.06.013.
[17] Y.J. Li, J. Zhang, Z.Y. Jia, et al., Research on a novel parallel spoke piezoelectric 6-DOF heavy force/torque sensor, Mech. Syst. Signal Process. 36. 1 ((2013) 152–167, https://doi.org/10.1016/j.ymssp.2012.03.016.
[18] R. Liang, Q.M.Wang High, sensitivity piezoelectric sensors using flexible PZT thick-film for shock tube pressure testing, Sens. Actuators A: Phys. 235 (2015) 317–327, https://doi.org/10.1016/j. sna.2015.09.027.
[19] Y. Sujan, G. Uma, M. Umapathy, Design and testing of piezoelectric resonant pressure sensor, Sens. Actuators, A 250 (2016) 177–186, https://doi.org/10.1016/ j.sna.2016.09.031.
[20] Y.J. Li, J. Zhang, Z.Y. Jia, et al., Research on force-sensing element's spatial arrangement of piezoelectric six-component force/torque sensor, Mech. Syst. Signal Process. 23. 8 ((2009) 2687–2698, https://doi.org/10.1016/j. ymssp.2009.05.014.
[21] Z.Y. Jia, S. Lin, W. Liu, Measurement method of six-axis load sharing based on the Stewart platform, Meas. 43. 3 ((2010) 329–335, https://doi.org/10.1016/j. measurement.2009.11.005.
[22] Y.J. Li, et al., A novel parallel piezoelectric six-axis heavy force/torque sensor, Meas. 42. 5 ((2009) 730–736, https://doi.org/10.1016/j. measurement.2008.12.005.
[23] Y.J. Li, et al., Research on the parallel load sharing principle of a novel self-decoupled piezoelectric six-dimensional force sensor, ISA Trans. 70 (2017) 447–457, https://doi.org/10.1016/j. isatra.2017.07.008.
[24] J. Liu, et al., Active design method for the static characteristics of a piezoelectric six-axis force/torque sensor, Sens. 14. 1 ((2014) 659–671, https://doi.org/ 10.3390/s140100659.
[25] M.Y. Xia, C.B. Zhou, et al., A dynamic disturbance force measurement system based on array sensor for large moving device in spacecrafts, J. Sound Vib. (2022), 117069, https://doi.org/10.1016/j.jsv.2022.117069.
[26] D.K. Gupta, A.K. Dhingra, Input load identification from optimally placed strain gages using D-optimal design and model reduction, Mech. Syst. Signal Process. 40 (2) (2013) 556–570, https://doi.org/10.1016/ j.ymssp.2013.06.011.
[27] D.K. Gupta, A.K. Dhingra. A reduced modal parameter based algorithm to estimate excitation forces from optimally placed accelerometers, Inverse Probl. Sci. Eng. 25 (3) (2017) 397–417, https://doi.org/10.1080/ 17415977.2016.1169276.
[28] D.K. Gupta, A.K. Dhingra. Dynamic programming approach to load estimation using optimal sensor placement and model reduction. Int J Comput Methods 15(3): 1850071. https://doi.org /10.1142/S0219876218500718.
[29] Z. Galil, J. Kiefer, Time- and space-saving computer methods, related to Mitchell's DETMAX, for finding D-Optimum designs, Technometrics 22 (1980) 301–313, https://doi.org/10.1080 /00401706.1980.10486161.
[30] X. Wang, Z. Xu, M. Xia, et al., Research on a six-degree-of-freedom disturbance force and moment simulator for space micro-vibration experiments, J. Sound Vibr 432 (2018) 530–548, https://doi.org/10.1016/j.jsv.2018.06.056.